Enhancement of Microwave Absorption Properties of Hexaferrite/Epoxy Composites on the Addition of Non-magnetic Oxides

Abanti Nag[1,*], Venu KS[2], Hema Singh[2]

1. Materials Science Division, CSIR-National Aerospace Laboratories, Bangalore, India
2. Centre for Electromagnetics, CSIR-National Aerospace Laboratories, Bangalore, India
Email: abanti@nal.res.in (Corresponding author)

Abstract: The effect of non-magnetic oxides such as Al_2O_3, TiO_2 and ZnO on the microwave absorption properties of magnetoplumbite barium hexaferrite ($BaFe_{11.8}Co_{0.2}O_{19}$) is analyzed. Barium hexaferrite nanoparticles are synthesized through the sol-gel auto-combustion method. $BaFe_{11.8}Co_{0.2}O_{19}$-$Al_2O_3$, $BaFe_{11.8}Co_{0.2}O_{19}$-$TiO_2$ and $BaFe_{11.8}Co_{0.2}O_{19}$-ZnO composites are synthesized in a 1:1 ratio through mechanical mixing and heat treatment. The epoxy composites are fabricated with 50% loading of $BaFe_{11.8}Co_{0.2}O_{19}$-$Al_2O_3$, $BaFe_{11.8}Co_{0.2}O_{19}$-$TiO_2$ and $BaFe_{11.8}Co_{0.2}O_{19}$-ZnO in epoxy matrix followed by room temperature curing. The powder XRD analyses showed homogeneous distribution of $BaFe_{11.8}Co_{0.2}O_{19}$ and Al_2O_3 in $BaFe_{11.8}Co_{0.2}O_{19}$-$Al_2O_3$ composite while TiO_2 and ZnO phases dominate in $BaFe_{11.8}Co_{0.2}O_{19}$-$TiO_2$ and $BaFe_{11.8}Co_{0.2}O_{19}$-ZnO composites, respectively. Scanning electron microscopy shows the evenly distributed $BaFe_{11.8}Co_{0.2}O_{19}$ and Al_2O_3 in $BaFe_{11.8}Co_{0.2}O_{19}$-$Al_2O_3$ composites. The electromagnetic characterization calculated from experimental permittivity and permeability shows reflection loss $R_L \leq$ -10 dB ($\geq$ 90% absorption) for a very small thickness of 0.5 mm over the entire *X*-band (8-12 GHz) for $BaFe_{11.8}Co_{0.2}O_{19}$-$Al_2O_3$ composites. $BaFe_{11.8}Co_{0.2}O_{19}$-$TiO_2$ and $BaFe_{11.8}Co_{0.2}O_{19}$-ZnO show $R_L <$ - 8 dB with a thickness of 2.5 mm over the frequency range 8–9.7 GHz and $R_L <$ - 8 dB with a thickness of 3.6 mm over 8.7-11.1 GHz, respectively. Further, when compared with $BaFe_{11.8}Co_{0.2}O_{19}$ alone ($R_L <$ -7 dB at 3.2 mm in 8-11 GHz), the $BaFe_{11.8}Co_{0.2}O_{19}$-$Al_2O_3$ composite is superior both in terms of the thickness of the coating as well as the percentage absorption in the *X*-band.
Keywords: Barium hexaferrite; Alumina; Titania; Zinc oxide; Electromagnetic absorption; X-band.

1. Introduction

Electromagnetic (EM) wave radiation in the gigahertz (GHz) range is the frequency for wireless communication tools and localized network systems and has been extensively used in recent days. The excessive use of EM waves in industrial, commercial and military applications is causing electromagnetic interference (EMI) pollution which is hazardous for human health. On one hand, electromagnetic interference pollution deteriorates the lifetime of communication devices e.g. cell phones, laptops and Bluetooth gadgets, commercial appliances e.g. microwave ovens and integrated electrical circuits present in automobiles. On the other hand, electromagnetic interference pollution causes several health problems such as anxiety, headache, sleeping disorder, etc. Electromagnetic wave absorption materials can absorb the microwave radiation energy generated from communication devices, commercial appliances and others and thereby attracted considerable attention as a promising candidate to replace metallic materials [1-5].

The fundamental of the electromagnetic absorbing materials is to successfully decrease the reflection of electromagnetic signals over the wide frequency range. The microwave absorber materials should absorb in the wide frequency range and sufficiently tough in a small thickness of materials. Therefore, the absorbing material should be such that the incident wave can penetrate the absorber material by a larger degree, i.e. zero reflection (impedance matching characteristics) and the electromagnetic wave inflowing the material should be entirely attenuated and absorbed within the limited depth of the materials, i.e. zero transmission (attenuation characteristics) [1].

The microwave absorption of absorbing materials is determined by complex permittivity (ε_r) and complex permeability (μ_r) that describes the interaction of absorbing materials with an electric field ($\varepsilon_r = \varepsilon' + j\varepsilon''$; $\tan \delta_\varepsilon = \frac{\varepsilon'}{\varepsilon''}$) and magnetic field ($\mu_r = \mu' + j\mu''$; $\tan \delta_\mu = \frac{\mu'}{\mu''}$), respectively, where ε' and μ' are the real part, ε'' and μ'' are the imaginary part and *tan δ* represents the loss tangent. The principle of an electromagnetic wave absorber is determined by the reflection loss (R_L) that is to develop the reflection reduction by impedance matching.

The mechanism of reflection loss is governed by dielectric loss and magnetic loss. Dielectric loss happens due to polarization relaxation and conduction loss, whereas, magnetic loss occurs due to eddy current effect, natural resonance and domain wall resonance. The proper combination between dielectric and magnetic losses is the precondition to achieve efficient microwave absorption [6].

M-type barium ferrite is the best candidate material as electromagnetic absorption in the microwave region, due to high Curie temperature ($T_C \sim 723$ K), high saturation magnetization (72 emu/g), high coercivity (0.67 T), high uni-axial magnetic anisotropy (17.2 kOe) along c-axis and high microwave magnetic loss and excellent chemical stability [7-10]. The external doping at Ba^{2+} and Fe^{3+} sites of hexagonal ferrite further improves the magnetization and the magnetic anisotropy of barium hexaferrite. The effect of single doping [11-17] by transition metal ions and a few rare-earth ions and co-doping [18-26] by a combination of them are investigated. While Fe^{3+} is substituted by non-magnetic ions such as the Zn^{2+} tetrahedral position, it produces a domain that opposes the magnetic moment at the octahedral position causing an increase in saturation magnetization and a decrease in the coercive field. On the other hand, the substitution of Fe^{3+} by magnetic ion e.g. Co^{2+} with 3 μB magnetic moments, causes a decrease in both saturation magnetization and coercive field. The lower effective magnetic moment of Co^{2+} (3 μB) in comparison with Fe^{3+} (5 μB) is the reason behind the decrease in saturation magnetic moment due to Co-doping. Further, the lower positive charge on Co^{2+} in comparison with Fe^{3+} causes a reduction in crystal field strength and magnetic interaction among the magnetic ions resulting in the low coercive field in Co-substituted barium hexaferrite.

We have explored the effect of particle size on magnetic and electromagnetic properties of Co-doped Barium hexaferrite ($BaFe_{11.8}Co_{0.2}O_{19}$) that showed broader absorption in the range of 8-18 GHz (*X*-band) with $R_L \leq$ -7 db for the samples with particles size $\leq$ 20 nm [27]. In this paper, we report the effect of non-magnetic oxides as additional filler on the electromagnetic properties of barium hexaferrite. The effect on microwave absorption of barium hexaferrite on the inclusion of highly insulating Al_2O_3, high dielectric TiO_2 and conducting ZnO is explored in non-magnetic oxide/epoxy composites of $BaFe_{11.8}Co_{0.2}O_{19}$-$Al_2O_3$, $BaFe_{11.8}Co_{0.2}O_{19}$-$TiO_2$ and $BaFe_{11.8}Co_{0.2}O_{19}$-$ZnO$, respectively.

2. Experimental details

2.1 Synthesis

For the synthesis of $BaFe_{11.8}Co_{0.2}O_{19}$, high purity precursors $Ba(NO_3)_2$ (Alfa Aesar, 99%), $Fe(NO_3)_3.9H_2O$ (Alfa Aesar, 98%), $Co(NO_3)_2.6H_2O$ (Sigma Aldrich, 98%) and citric acid (Alfa Aesar, 99.5%) were used. The polycrystalline powder of $BaFe_{11.8}Co_{0.2}O_{19}$ (BFC) was prepared by the sol-gel auto-combustion method. An aqueous solution of the above metal nitrates was mixed with citric acid with metal to the citric acid molar ratio of 1:1 to form the sol with pH<1, which resulted in gel formation upon boiling at 353 K. While the temperature was raised to 423 K, auto-combustion took place with the ignition of viscous gel followed by the formation of the ferrite particles. The powder was ground and kept at 773 K for 3 hours in the muffle furnace, followed by 1073 K for 5 hours and 1473 K for 3 hours with several intermittent grinding. The described process produced $BaFe_{11.8}Co_{0.2}O_{19}$ [27].

For the preparation of the composites of $BaFe_{11.8}Co_{0.2}O_{19}$-$Al_2O_3$ (BFC-A), $BaFe_{11.8}Co_{0.2}O_{19}$-$TiO_2$ (BFC-T) and $BaFe_{11.8}Co_{0.2}O_{19}$-$ZnO$ (BFC-Z), high purity oxides Al_2O_3 (Alfa, Aesar, 99%), TiO_2 (Alfa Aesar, 99.5%) and ZnO (Alfa Aesar, 99.99%) were used. The BFC-A, BFC-T and BFC-Z composites were prepared with a 1:1 ratio of BFC and other oxides in each case. The mixture of BFC and other oxide were ground in mortar pestle for several hours. Ethanol was used as grinding media for effective and homogeneous mixing. After milling, the powder was dried in the oven at 100 ºC. The dried powder was annealed at 700 ºC for 5 hours to form the composites of BFC-A ($BaFe_{11.8}Co_{0.2}O_{19}$-$Al_2O_3$), BFC-T ($BaFe_{11.8}Co_{0.2}O_{19}$-$TiO_2$) and BFC-Z ($BaFe_{11.8}Co_{0.2}O_{19}$-$ZnO$).

For electromagnetic characterization, BFC-A/epoxy, BFC-T/epoxy and BFC-Z/epoxy composites were fabricated. The epoxy composites were fabricated using the epoxy resin Araldite LY5052 as the matrix material, whereas Aradur LY5052 was used as the curing agent. Epoxy resin and curing agent in the weight ratio of 10:3 were used to obtain the complete polymerization. Metal oxides of BFC-A, BFC-T and BFC-Z were distributed uniformly in the epoxy resin with 50% loading under constant mixing and degassing under vacuum to remove the bubbles. The prepared slurry was then mixed with a curing agent and poured in a rectangular mould of dimension square block of 25 mm × 25 mm × 5 mm and degassing under vacuum is continued to remove the bubbles. The samples were post cured at room temperature for a few days before being taken for characterization.

2.2 Characterization

The phase determination was done through powder *x*-ray diffraction on M/s. Bruker D8 Advance *x*-ray diffractometer with Ni-filtered Cu *Kα* radiation. The morphology of the powder samples was investigated by scanning electron microscopy (SEM) using a Carl Zeiss EVO18 SEM. The EM material characterization measurements were carried out to extract the complex permittivity and permeability (ε'-$i\varepsilon''$, μ'-$i\mu''$) of the BFC

composites in the desired frequency range of 8–12 GHz. It is well known that the permittivity and permeability of a material are essentially a result of the electronic, ionic, and intrinsic electric dipole polarization, and associated magnetic properties. Moreover, these parameters depend on the size, structure, and geometrical morphology of the material. It was a waveguide system having a sample holder with specific dimensions as per the frequency range. The vector network analyzer was used to measure *S*-parameters and hence the permittivity and permeability of the material sample. The dimension of the pellets used for *X*-band (8-12 GHz) was 22.93 mm × 10.19 mm × 5.08 mm.
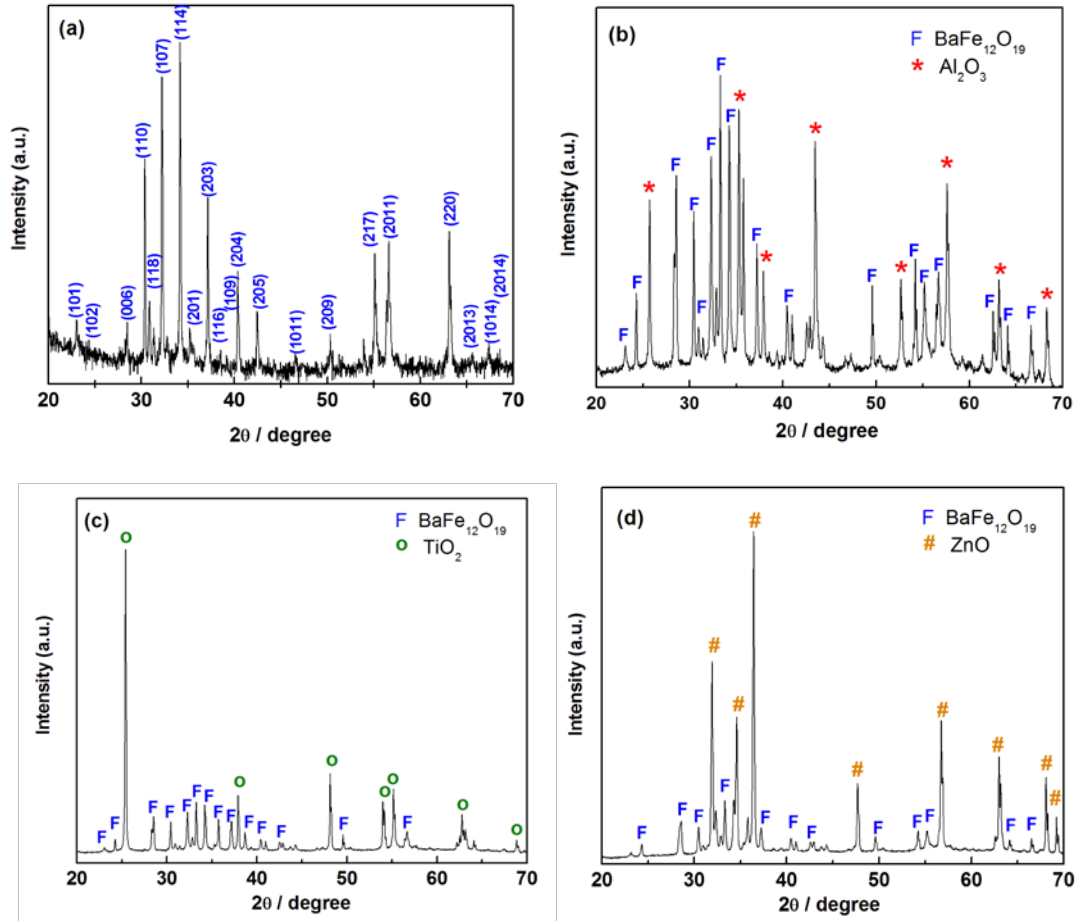
Figure 1. XRD pattern of (a) $BaFe_{11.8}Co_{0.2}O_{19}$ (BFC) nano-powder, (b) BFC-Al_2O_3 composite, (c) BFC-TiO_2 composite and (d) BFC-ZnO composite.

3. Results and discussion

3.1 Powder X-Ray diffraction analyses

The XRD patterns of BFC, BFC-A, BFC-T and BFC-Z composites are shown in Figure 1. Figure 1a shows powder x-ray diffraction patterns BFC ($BaFe_{11.8}Co_{0.2}O_{19}$) that is found to be phase pure. Most of the peaks are indexed as *M*-type barium hexaferrite with $P6_3/mmc$ space group (PCD No. 1714630). This along with the TEM micrographs (Figure 2) concludes the formation of phase pure barium hexaferrite nano-particles [27]. Figure 1b shows the XRD pattern of BFC-A ($BaFe_{11.8}Co_{0.2}O_{19}$-$Al_2O_3$). The BFC-A XRD patterns display all the crystal planes attributed to the crystal structure of *M*-type barium hexaferrite (PCD No. 1714630) along with all the peaks of the rhombohedral system of α-Al_2O_3 with space group *R-3c*, e.g. (012), (104), (110), (113), (024), (116), (214) and (300) (JCPDS File No. 85-1337). The absence of any other phase indicates the composite formation of $BaFe_{11.8}Co_{0.2}O_{19}$-$Al_2O_3$.

Figure 1c exemplifies the diffractogram of sintered powder of BFC-T ($BaFe_{11.8}Co_{0.2}O_{19}$-$TiO_2$) pertaining to BFC and TiO_2 in a 1:1 ratio. Similar to BFC-A, all the observed peaks of the x-ray diffraction patterns can be indexed with the *M*-type barium hexaferrite system with space group $P6_3/mmc$ and tetragonal TiO_2 (JCPDS File No. 86–1157) with space group $I4_1/amd$. The sharp and strong peaks of stable tetragonal TiO_2 phase are present and signify that the samples have crystalline phase, and no other phases of TiO_2 are observed. The predominant

peaks of TiO_2 in comparison with BFC exhibit a higher scattering phenomenon of TiO_2 rich zone in comparison with BFC rich one.

The composition of the BFC-Z ($BaFe_{11.8}Co_{0.2}O_{19}$-ZnO) composite is studied by XRD pattern and it is represented in Figure 1d. It is validated the presence of both *M*-type barium hexaferrite and wurtzite ZnO (JCPDS No. 80–0075) with space group *P6$_3$mc* in the XRD pattern. Similar to BFC-T, the more intense peaks of ZnO in comparison with BFC indicate the higher scattering phenomenon of ZnO-rich zone in comparison with BFC-rich one.

On closure look on the powder XRD pattern of BFC-A, BFC-T and BFC-Z, it can be observed that, in BFC-A, there is a homogeneous distribution of hexaferrite and alumina phases in the composite matrix. However, in both the cases of BFC-T and BFC-Z, the TiO_2 and ZnO phases predominate, respectively.
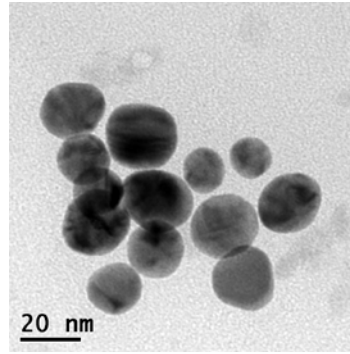

Figure 2. Low resolution transmission electron microscopy (LRTEM) image of BFC

3.2 Scanning Electron Microscopy (SEM) analyses

Figure 3 shows the scanning electron micrograph of BFC-A, BFC-T and BFC-Z composites and the corresponding EDX recorded to understand the composition of the composites as shown in the inset. The SEM images of the BFC-A composite show well distribution of Al_2O_3 plates and $BaFe_{11.8}Co_{0.2}O_{19}$ nanoparticles (Figure 3a). In agreement with the XRD pattern, the SEM images confirm the homogeneous distribution of hexaferrite and alumina in the BFC-A composites.
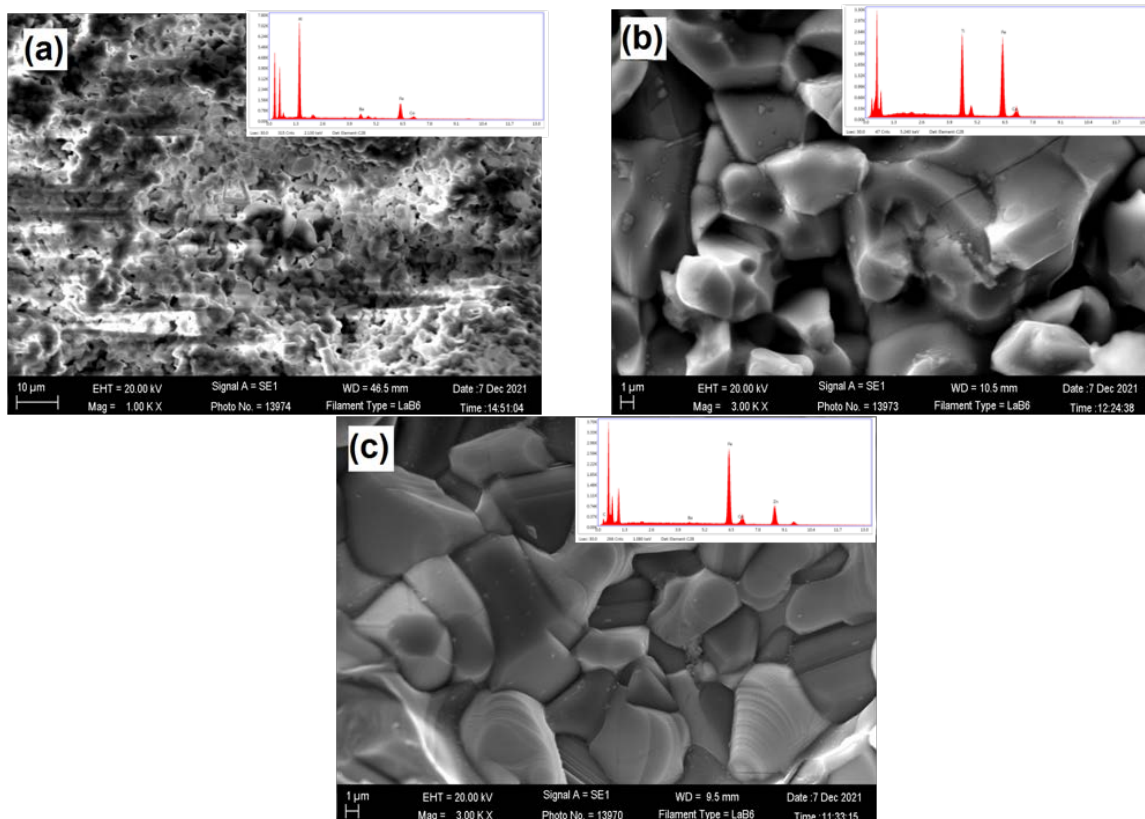

Figure 3. SEM micrograph of (a) BFC-Al2O3, (c) BFC-TiO2 and (d) BFC-ZnO composites. Inset shows the EDX of (a) BFC-Al2O3, (c) BFC-TiO2 and (d) BFC-ZnO composites, respectively

The SEM image of the BFC-T composite shows the $BaFe_{11.8}Co_{0.2}O_{19}$ nanoparticles evenly distributed all around the TiO_2 particles. It is clear from the morphology that BFC-T composites have TiO_2 matrix as the major component with particle size ranging from 2-10 μm (Figure 3b). BFC-Z composite also shows similar features like BFC-T (Figure 3c). The hexagonal nano-platelet of Ba-hexaferrite is evenly distributed in the columnar wurtzite grains of ZnO.

3.3 Electromagnetic wave absorbing properties

The complex permittivity (ε', ε'') and permeability (μ', μ'') spectra of BFC-A, BFC-T and BFC-Z are plotted as a function of frequency along with BFC for comparison in the frequency range of 8-12 GHz. The real part of complex permittivity and permeability are mainly related to the extent of polarization happening in the material and it implies the storage ability of the electric and magnetic energy. On the other hand, the imaginary part of permittivity and permeability accounts for dielectric and magnetic loss, respectively [1]. The complex permittivities ($\varepsilon_r = \varepsilon' - j\varepsilon''$), complex permeabilities ($\mu_r = \mu' - j\mu''$), dielectric loss tangent ($tan\,\delta_\varepsilon = \varepsilon''/\varepsilon'$) and magnetic loss tangent ($tan\,\delta_\mu = \mu''/\mu'$) spectra in 8-12 GHz for BFC-A/epoxy, BFC-T/epoxy and BFC-Z/epoxy composites are shown at Figure 4, Figure 5 and Figure 6, respectively, in comparison with BFC-epoxy composite.
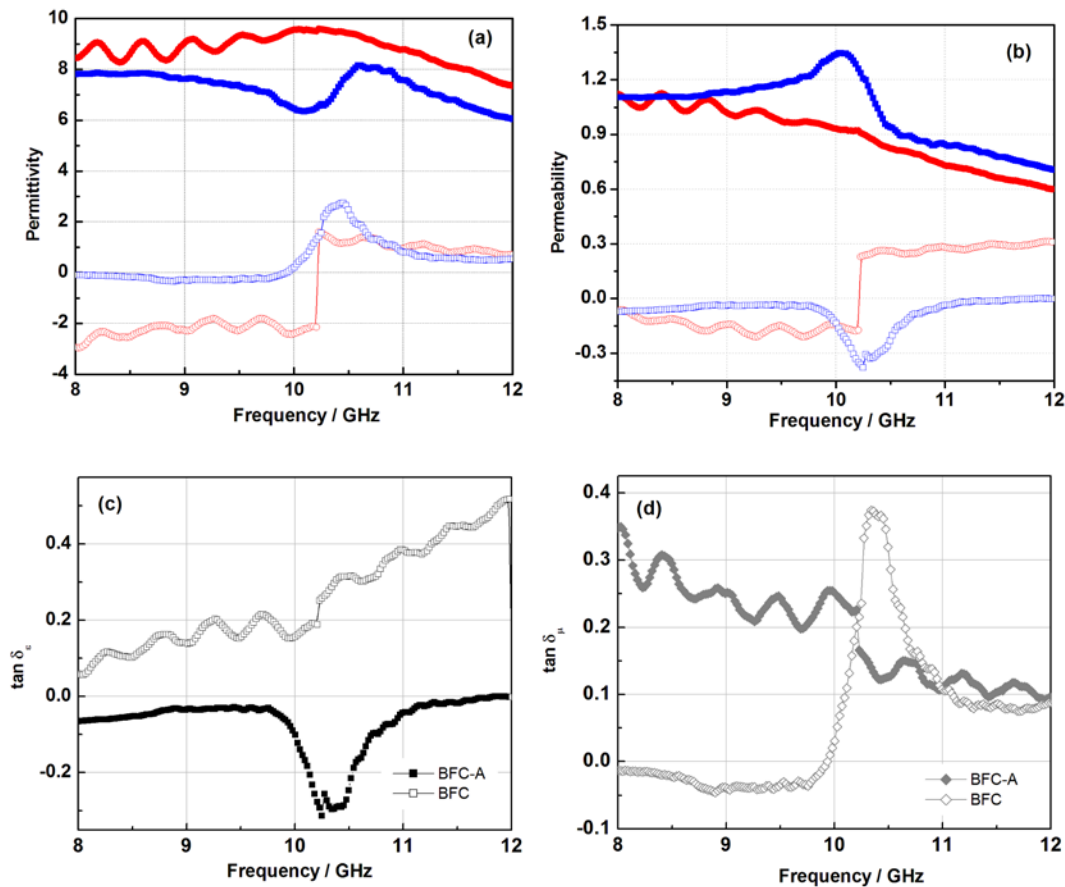

Figure 4. Measured (a) permittivities and (b) permeabilities in 8-12 GHz for BFC-Al_2O_3 compositions (red solid and open symbol) in comparison with (a) permittivities and (b) permeabilities of BFC (blue solid and open symbol) where solid symbols and open symbols represent real and imaginary parameters. The (c) dielectric loss tangent (tan δ_ε) and (d) magnetic loss tangent (tan δ_μ) spectra for BFC-A in comparison with BFC.

The real part of the complex permittivity of BFC-A is slightly higher than that of BFC while the imaginary part is slightly less up to 10.3 GHz and then equalizes (Figure 4a). This may be because of incorporation of insulating Al_2O_3 phases in the BFC-A composite. The ε' is consistent with the frequency indicating that polarization of the dielectric dipole and oscillation of the electric field vector is in-phase with each other. The ε'' is initially consistent with the frequency but suddenly increases at 10.3 GHz. This could be associated with the loss process through the oscillation of the dipoles [28]. Actually, dielectric loss undergoes different loss mechanisms with the increase of frequencies. At low frequency, the loss is calculated by the leak conductance and is independent of the frequency. At microwave frequency, the dielectric losses are associated with electric conductance and relaxation polarization loss. Therefore, the increase in the imaginary component of the permittivity may be the outcome of the increase of the electric conductance loss as well as the relaxation polarization loss. BFC has a better dielectric loss (*tan* δ_ε)

than BFC-A composites (Figure 4c). The real part of the complex permeability of BFC-A is slightly lower than that of BFC while the imaginary part supersedes BFC above 10 GHz (Figure 4b). The lower value of μ' in the case of BFC-A is due to the incorporation of non-magnetic Al_2O_3 in the magnetic ferrite matrix of BFC. Further, it is observed that μ' gradually decreases as frequency increases that may be because of domain wall motion and relaxation. The magnetic loss (*tan δ_μ*) of BFC-A is better than BFC (Figure 4d). The peak observed at 10.3 GHz for BFC-A in both the imaginary part of permittivity and permeability can be attributed to domain wall displacement between BFC and Al_2O_3 grains. This phenomenon is reflected in the dielectric and magnetic loss spectra also.
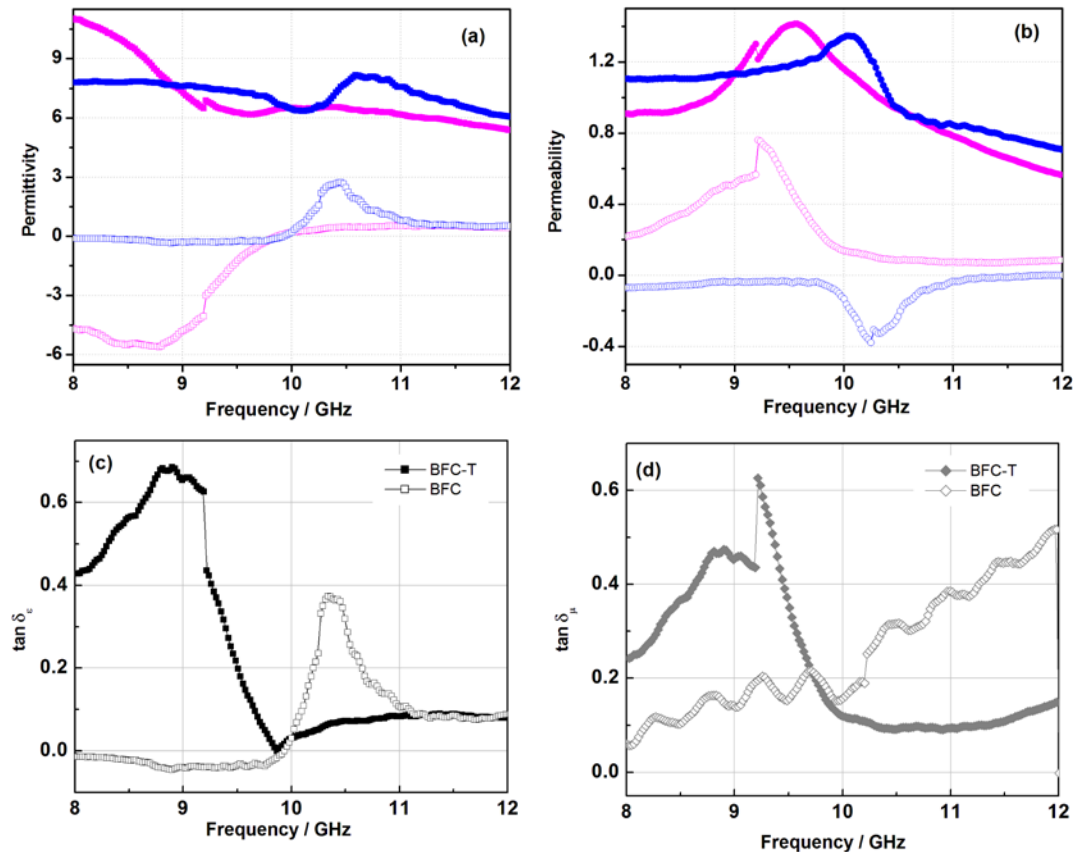

Figure 5. Measured (a) permittivities and (b) permeabilities in 8-12 GHz for BFC-TiO$_2$ compositions (magenta solid and open symbol) in comparison with (a) permittivities and (b) permeabilities of BFC (blue solid and open symbol) where solid symbols and open symbols represent real and imaginary parameters. The (c) dielectric loss tangent (tan δ_ε) and (d) magnetic loss tangent (tan δ_μ) spectra for BFC-T in comparison with BFC.

In the case of BFC-T, both the real and imaginary parts of the complex permittivity of BFC-T are slightly lower than that of BFC (Figure 5a). On the other hand, BFC-T has a better dielectric loss (*tan δ_ε*) than BFC up to 10 GHz (Figure 5c). The incorporation of highly dielectric material TiO_2 in BFC-T composite is the probable reason behind it. The real part of the complex permeability of BFC-T is almost equivalent to BFC while the imaginary part is higher (Figure 5b). The magnetic loss (*tan δ_μ*) of BFC-T is also better than BFC up to 10 GHz (Figure 5d). The peak observed at 9.3 GHz for BFC-T in both the real and imaginary part of permeability can be ascribed to magnetic resonance and domain wall motion. This phenomenon is reflected in the magnetic loss spectra also.

On the other hand, both the real and imaginary parts of the complex permittivity of BFC-Z are slightly higher than that of BFC (Figure 6a) up to 10.5 GHz. The increase in complex permittivities due to the incorporation of ZnO is related with interfacial polarization arising from the accumulation of charge carriers at the interface region. According to Maxwell–Wagner effect, the reason behind the interfacial polarization is the accumulation of charge carriers between two components of the composites having varying dielectric constants and conductivity [29]. The incorporation of conducting ZnO in BFC-Z composite produces heterogeneous interfaces that enhance the dielectric permittivity. Further, according to free-electron theory, ε'' is inversely proportional to resistivity and frequency. Conducting oxide ZnO forms a conducting net when introduced into the BFC-Z composites that lead to lower resistivity leading to higher ε''. This is reflected in the dielectric loss factor where BFC-Z has a better dielectric loss (*tan δ_ε*) than BFC up to 10 GHz (Figure 6c). The real part of the complex permeability of BFC-Z is

slightly lower than BFC while the imaginary part is higher (Figure 6b). The magnetic loss (*tan δ_μ*) of BFC-Z is also better than BFC up to 10 GHz (Figure 6d).
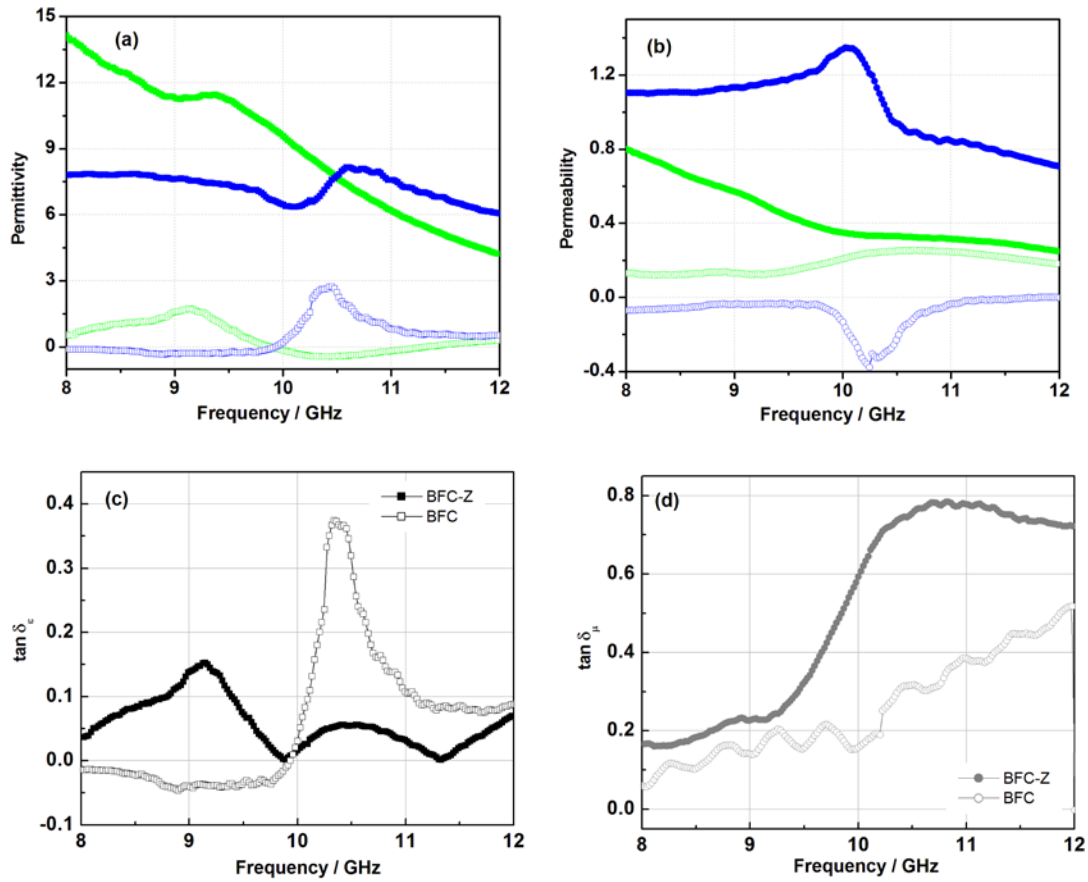

Figure 6. Measured (a) permittivities and (b) permeabilities in 8-12 GHz for BFC-ZnO compositions (green solid and open symbol) in comparison with (a) permittivities and (b) permeabilities of BFC (blue solid and open symbol) where solid symbols and open symbols represent real and imaginary parameters. The (c) dielectric loss tangent (tan δ$_\varepsilon$) and (d) magnetic loss tangent (tan δ$_\mu$) spectra for BFC-Z in comparison with BFC.

3.4 The reflection loss

The principle of microwave absorption of a material is governed by two important factors; good impedance matching characteristics and a strong attenuation capability. The attenuation capability of the material is closely related to complex permittivity, complex permeability, thickness, conductance and the structure of the absorber. This eventually helps EM waves to penetrate the materials efficiently with minimal reflection at the interfaces. The reflections from the surface of the absorber are minimized if the characteristic impedance of the absorber is close to the free space impedance. Reflection loss (R_L) correlates the impedance matching characteristics and attenuation capability of the absorber material. The reflection loss (R_L) of electromagnetic waves was calculated from the relative permeability and permittivity at the specified frequency and absorber thickness as follows [1,6]:

$$Z_1 = \sqrt{\frac{\mu_r}{\varepsilon_r}} tanh \left[j \frac{2\pi f d}{c} \sqrt{\mu_r \varepsilon_r} \right]$$

$$R_L = -20 log \left| \frac{Z_1 - Z_0}{Z_1 + Z_0} \right|$$

where, Z_1 is material impedance, Z_0 is the impedance of free space, *f* is frequency of the electromagnetic wave, *d* is thickness of an absorber and *c* is the velocity of light.

To analyze the reflection coefficient (dB) of the developed BFC-A, BFC-T and BFC-Z composites for *X*-band frequencies (8-12 GHz), the material layer is placed over the perfect electric conductor (PEC) plate. Since the transmission through the PEC plate would be negligible, one can relate the absorption performance of the coating in terms of the reflection coefficient. We have reported previously, BFC alone with a coating thickness of 3.2 mm shows R_L < -7 dB in 8-11 GHz which corresponds to the absorption close to 80% [27]. Figure 7 shows the reflection

coefficient (dB) of BFC-A, BFC-T and BFC-Z composites simulated from the experimental permittivity and permeability. It is apparent that the material BFC-A shows low reflection for a very small thickness of 0.5 mm over the entire X-band. The $R_L \leq$ -10 dB corresponds to the absorption of 90% or more for the incident electromagnetic (EM) waves. On the other hand, the BFC-T shows $R_L <$ -8 dB with a thickness of 2.5 mm over a narrow frequency range 8–9.7 GHz which corresponds to the absorption greater than 80%. Similarly, BFC-Z shows reflection $R_L <$ -8 dB with a thickness of 3.6 mm over a narrow frequency range of 8.7 to 11.1 GHz. Table 1 summarizes the results of reflection loss of the developed composites in comparison with BFC alone. The corresponding absorption performance of the materials is shown in Figure 8. Therefore, the reflection coefficient analysis conclude that BFC-A performs better in much lower thickness and results in absorption of 90% or more for the entire X-band frequencies. This can easily be correlated with the structural analyses that show homogeneous distribution of insulating Al_2O_3 and magnetic $BaFe_{11.8}Co_{0.2}O_{19}$ phases in BFC-A composite according to powder XRD and SEM micro-structural analysis. Further, when compared with BFC alone, the BFC-A is superior both in terms of the thickness of the coating as well as the percentage absorption in the X-band. The absorption of BFC-A composite ($R_L \leq$ -10 dB at thickness of 0.5 mm) is 10% higher than BFC alone ($R_L <$ -7 dB at thickness of 3.2 mm) in 8-12 GHz in much lower thickness [27]. Therefore, it can be concluded that the addition of insulating Al_2O_3 in the Ba-hexaferrite matrix drastically improves the electromagnetic absorption properties at a nominal thickness (less weight penalty) of coating and therefore BFC-A can be considered as a potential candidate of radar absorbing material for stealth applications.
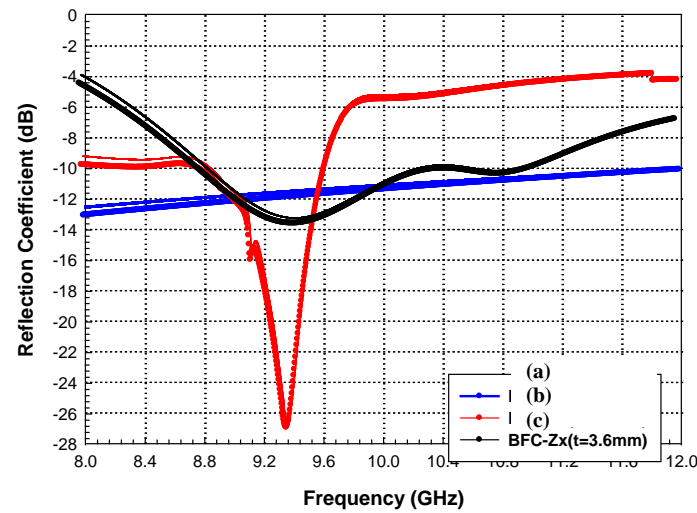

Figure 7. Reflection coefficient of the developed materials coating over conducting plate with different thickness (a) BFC-Al_2O_3, coating thickness = 0.5 mm, (b). BFC-TiO_2, coating thickness = 2.5 mm and (c) BFC-ZnO, coating thickness = 3.6 mm.
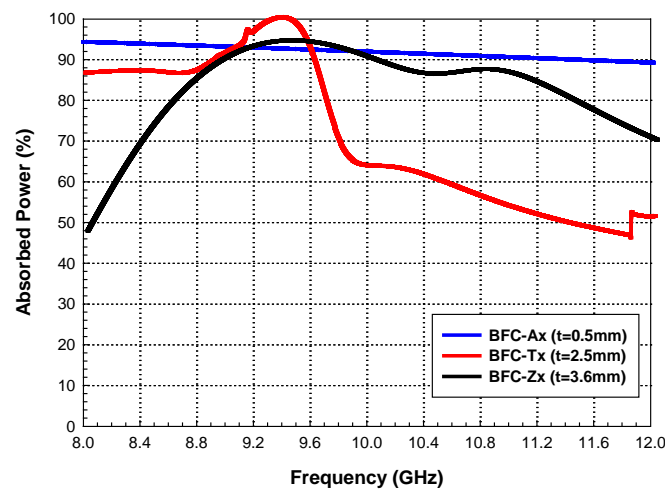

Figure. 8. Absorption performance of (a) BFC-Al_2O_3, (c) BFC-TiO_2 and (d) BFC-ZnO composites in X-band

Table 1. The reflection loss, percentage absorption and thickness of the material

Compositions	Reflection loss (R_L) (dB)	% Absorption	Frequency (GHz)	Thickness (mm)
$BaFe_{11.8}Co_{0.2}O_{19}$-$Al_2O_3$	$\leq$ -10	$\geq$ 90	8 – 12	0.5
$BaFe_{11.8}Co_{0.2}O_{19}$-$TiO_2$	< -8	> 84	8 – 9.7	2.5
$BaFe_{11.8}Co_{0.2}O_{19}$-ZnO	< -8	> 84	8.7 – 11.1	3.6
$BaFe_{11.8}Co_{0.2}O_{19}$	< -7	> 80	8 – 11	3.2

4. Conclusions

In this paper, we have discussed how the presence of non-magnetic oxides such as insulating Al_2O_3, highly dielectric TiO_2 and conducting ZnO affect the magnetic and electromagnetic properties of Co-doped barium hexaferrite. Incorporation of non-magnetic oxide in the ferrite matrix causes composite formation where there is equal distribution of heterogeneous phases in the case of $BaFe_{11.8}Co_{0.2}O_{19}$-$Al_2O_3$. On the other hand, TiO_2 and ZnO phases predominate for $BaFe_{11.8}Co_{0.2}O_{19}$-$TiO_2$ and $BaFe_{11.8}Co_{0.2}O_{19}$-ZnO composites, respectively. This correlates well with the electromagnetic properties of $BaFe_{11.8}Co_{0.2}O_{19}$-$Al_2O_3$, which shows reflection loss $\leq$ -10 dB ($\geq$ 90% absorption) for a very small thickness of 0.5 mm over the entire X-band. Further, $BaFe_{11.8}Co_{0.2}O_{19}$-$Al_2O_3$ composite not only over perform the other two composites, it also proves superior to $BaFe_{11.8}Co_{0.2}O_{19}$ nanoparticles both in terms of the thickness of the coating as well as the percentage absorption in the *X*-band.

Acknowledgments

5. References

[1] Vinoy K J, Jha R M. Trends in radar absorbing materials technology. Sadhana. 1995;20: 815-850.
[2] Saville P. Review of radar absorbing materials. DRDC Atlantic TM. 2005;003. https://asset-pdf.scinapse.io/prod/1572438051/1572438051.pdf
[3] Qin F, Brosseau C. A review and analysis of microwave absorption in polymer composites filled with carbonaceous particles. Journal of Applied Physics. 2012;111: 061301.
[4] Kapelewski J. On current and prospective use of binary thin multilayers in radar absorbing structures. Acta Physica Polonica A. 2013;124: 451-455.
[5] Aytaç A, İpek H, Aztekin K, Aytav E, Çanakçı B. A review of the radar absorber material and structures. Scientific Journal of the Military University of Land Forces. 2020;52: 931-946.
[6] Vinoy K J, Jha R M. Radar absorbing materials - from theory to design and characterization. 1996, Kluwer Academic Publishers, Springer US.
[7] Houbi A, Aldashevich Z A, Atassi Y, Telmanovna Z B, Saule M, Kubanych K. Microwave absorbing properties of ferrites and their composites: A review. Journal of Magnetism and Magnetic Materials. 2021;529: 167839.
[8] Pullar R C. Hexagonal ferrites: a review of the synthesis, properties and applications of hexaferrite ceramics. Progress in Materials Science. 2012;57: 1191-1334.
[9] Braun P B. Philips Research Reports. 1957;12: 491. https://www.pearl-hifi.com/06_Lit_Archive/ 02_PEARL_Arch/Vol_16/Sec_53/Philips_Rsrch_Reports_1946_thru_1977/Philips%20Research%20Repo rts-12-1957.pdf.
[10] Gorter E W. Philips Research Reports. 1954;9: 295. https://www.pearl-hifi.com/06_Lit_Archive/ 02_PEARL_Arch/Vol_16/Sec_53/Philips_Rsrch_Reports_1946_thru_1977/Philips%20Research%20Repo rts-09-1954.pdf.
[11] Obradors X, Collomb A, Pernet M, Samaras D, Joubert J C. X-ray analysis of the structural and dynamic properties of $BaFe_{12}O_{19}$ hexagonal ferrite at room temperature. Journal of Solid State Chemistry. 1985;56: 171-181.
[12] Pereira F M M, Junior C A R, Santos M R P, Sohn R S T M, Freire F N A, Sasaki J M, de Paiva J A C, Sombra A S B. Structural and dielectric spectroscopy studies of the M-type barium strontium hexaferrite alloys ($Ba_xSr_{1-x}Fe_{12}O_{19}$). Journal of Materials Science: Materials in Electronics. 2008;19: 627–638.

[13] Ghzaiel T B, Dhaoui W, Pasko Mazaleyrat A F. Effect of non-magnetic and magnetic trivalent ion substitutions on BAM-ferrite properties synthesized by hydrothermal method. Journal of Alloys and Compounds. 2016;671: 245-253.

[14] Kumar A, Kumar V, Ghumman S S. Synthesis and characterization of titanium doped barium ferrite and effects of doping on electrical and magnetic properties of the compound. Ferroelectrics. 2017;519: 82-89.

[15] Dairy A R A, Al-Hmoud L A, Khatabeh H A. Magnetic and structural properties of barium hexaferrite nanoparticles doped with titanium. Symmetry. 2019;11: 732.

[16] Araz I. Microwave charecterization of Co-doped barium hexaferrite absorber metarial. Journal of Superconductivity and Novel Magnetism. 2016;29: 1545-1550.

[17] Tran N, Choi Y J, Phan T L, Yang D S, Lee B W. Electronic structure and magnetic and electromagnetic wave absorption properties of $BaFe_{12-x}Co_xO_{19}$ M-type hexaferrites. Current. Applied Physics. 2019;19: 1343-1348.

[18] Araz I. Electromagnetic properties of Ce substituted barium hexaferrite in X-band frequencies. Journal of Materials Science: Materials in Electronics. 2019;30: 14935-14943.

[19] Behera P, Ravi S. Effect of Ni doping on structural, magnetic and dielectric properties of M-type barium hexaferrite. Solid State Science. 2019;89: 139-149.

[20] Cai S, Xin P H, Wang P F, Zhang B B, Han Y B, Peng X L, Hong B, Jin H X, Gong J, Jin D F, Ge H L, Wang X Q, Zhang J. The sol–gel synthesis of rare-earth ions substituted barium hexaferrites and magnetic properties. Modern Physics Letter B. 2013;27: 1350192-1-12.

[21] Trukhanov S V, Trukhanov A V, Kostishyn V G, Panina L V, Trukhanov A V, Turchenko V A, Tishkevich D I, Trukhanova E L, Yakovenko O S, Matzui L Y, Vinnik D A, Karpinsky D V. Effect of gallium doping on electromagnetic properties of barium hexaferrite. Journal of Physics Chemistry of Solids. 2017;111: 142-152.

[22] Zhao H, Du Y, Kang L, Xu P, Du L, Sun Z, Han X. Precursor-directed synthesis of quasi-spherical barium ferrite particles with good dispersion and magnetic properties. Crystal Engineering and Communication. 2013;15: 808-815.

[23] Mesdaghi S, Yousefi M, Sadr M H, Mahdavian A R. Effect of Sn^{4+}–Zn^{2+}–Co^{2+} doping on structural and magnetic properties of M-type barium hexaferrites. IEEE Transactions on Magnetics. 2019;55: 2100106.

[24] Feng Y B, Qui T, Shen C Y. Absorbing properties and structural design of microwave absorbers based on carbonyl iron and barium ferrite. Journal of Magnetism and Magnetic Materials. 2007;318: 8-13.

[25] Li W, Qiao X, Li M, Liu T, Peng H X. La and Co substituted M-type barium ferrites processed by sol–gel combustion synthesis. Materials Research Bulletin. 2013;48; 4449-4453.

[26] Tanwar K, Gyan D S, Gupta P, Pandey S, Prakash O, Kumar D. Investigation of Crystal Structure, Microstructure and Low Temperature Magnetic Behavior of Ce^{4+} and Zn^{2+} Co-Doped Barium Hexaferrites ($BaFe_{12}O_{19}$). RSC Advances. 2018;8: 19600-196009.

[27] Nag A, Bose R S C, Venu K S. Singh H. Influence of particle size on magnetic and electromagnetic properties of hexaferrite synthesised by sol-gel auto combustion route. Ceramic International. 2022;48: 15303-15313.

[28] Ohsato H, Verghese J, Jantunen H. Dielectric losses of microwave ceramics based on crystal structure, Electromagnetic Materials and Devices, Edited by M.-G. Han, 2018,

[29] Iwamoto M. Maxwell–Wagner Effect. In: Bhushan B. (eds) Encyclopedia of Nanotechnology. 2012, Springer, Dordrecht.